18th AIAA Computational Fluid Dynamics Conference
25 - 28 June 2007, Miami, FL

AIAA 2007-4323

High-Order Central ENO Finite-Volume Scheme with Adaptive Mesh Refinement

L. Ivan* and C.P.T. Groth†

University of Toronto Institute for Aerospace Studies

4925 Dufferin Street, Toronto, Ontario, M3H 5T6, Canada

A high-order central essentially non-oscillatory (CENO) finite-volume scheme in combination with a block-based adaptive mesh refinement (AMR) algorithm is proposed for solution of hyperbolic systems of conservation laws on body-fitted multi-block mesh. The CENO scheme is based on a hybrid solution reconstruction procedure that combines an unlimited high-order k-exact least-squares reconstruction technique following from a fixed central stencil with a monotonicity preserving limited piecewise linear reconstruction algorithm. Switching in the hybrid procedure is determined by a solution smoothness indicator that indicates whether or not the solution is resolved on the computational mesh. The hybrid approach avoids the complexity associated with other ENO schemes that require reconstruction on multiple stencils which in some cases can produce poorly conditioned coefficient matrices. A novel h-refinement criterion based on the solution smoothness indicator is used to direct the refinement of the AMR mesh. The predictive capabilities of the proposed high-order AMR scheme are demonstrated for the Euler equations governing two-dimensional compressible gaseous flows. The ability of the scheme to accurately represent solutions with smooth extrema and yet robustly handle under-resolved and/or non-smooth solution content (i.e., shocks and other discontinuities) is shown for a range of problems. Moreover, the ability to perform mesh refinement in regions of smooth but under-resolved and/or non-smooth solution content until the desired resolution is achieved is also demonstrated.

I. Introduction and Motivation

The potential of high-order methods to reduce the cost of numerical simulations is an active area of research, particularly for large-scale scientific computing applications such as direct numerical simulations (DNS) and large eddy simulations (LES) of turbulent non-reactive and combusting flows, numerical computation of complex unsteady aerodynamic flows, aeroacoustic modelling, and computational electromagnetics. Standard lower-order spatial discretizations (i.e., methods up to second order) can exhibit excessive numerical error and are therefore very often not practical for the applications listed above. Improved numerical efficiency may be achieved by raising the order of accuracy of the spatial discretization, thereby reducing the number of computational cells required to achieve the desired solution accuracy. Adaptive mesh refinement (AMR) is another approach for coping with the computational cost of large-scale numerical simulations. Computational grids that automatically adapt to the solution of the governing equations are very effective in treating problems with disparate length scales, providing the required spatial resolution while minimizing memory and storage requirements. For numerical simulations of physically complex flows having a wide range of spatial and temporal scales both high-order discretizations and AMR are demanded. For example, it is pointed out by Moin and Krishnan[1] that even ENO schemes as high as sixth-order can be too dissipative for the prediction of shock/turbulence interactions without refinement of the mesh around the shock wave. In other work, Jameson[2] has shown that high-order methods can be considerably more efficient than low-order AMR schemes for flows containing structures such as vortices, eddies and/or turbulence and concluded that high-order schemes combined with AMR may provide very effective means of obtaining high solution

*PhD Candidate, Email: lucian.ivan@utoronto.ca, Student Member AIAA.
†Associate Professor, Email: groth@utias.utoronto.ca, Senior Member AIAA.

accuracy. Moreover, even if a combination of high-order discretization and AMR can reduce significantly the cost of large-scale numerical simulations, a parallel implementation of these approaches is usually necessary in order to make the solution of such problems affordable on currently available hardware. Large massively parallel distributed memory computers can provide many fold increases in processing power and memory resources beyond those of conventional single-processor computers and would therefore provide another obvious avenue for greatly reducing the time required to obtain numerical solutions of large-scale scientific computing applications and/or physically complex flows. Thus, it is felt that the design of a high-order spatial discretization algorithm should be considered in the context of both mesh adaptation and parallel implementation of the algorithm.

In the last decade there have been a number of studies of high-order schemes for both hyperbolic conservation laws and compressible flow simulations. The challenge has been to achieve accurate discretizations while coping in a reliable and robust fashion with discontinuities and shocks. The ENO schemes first proposed by Harten *et al.*[3] provide robust frameworks for high-order discretizations of hyperbolic systems. The stencil leading to the "smoothest" reconstruction is selected and therefore stencils containing discontinuities are avoided. Abgrall[4] and Sonar[5] have since extended the ENO concept for application to flow prediction on unstructured mesh. In addition, so-called weighted ENO (WENO) schemes have been developed for both structured and unstructured mesh.[6–8] However, the difficulty with these approaches has been the extension of the method to multi-dimensional problems and large systems of coupled partial differential equations. The computational challenges are primarily related to the selection of stencils on multi-dimensional meshes, particularly in the case of unstructured grids,[4,5,9,10] and the poor conditioning of the linear systems that define the solution reconstructions for these stencils.[9,10] Although successful implementations have been developed, in general the computational costs and complexity of implementing ENO and WENO schemes have limited their widespread application. Despite these limitations, combinations of high-order ENO and WENO schemes with AMR for both structured and unstructured meshes have also been developed and applied to engineering problems such as the prediction of high-speed flow as described in the recent work by Wolf and Azevedo.[11]

Other researchers have considered more flexible high-order schemes, which may be more easily extended to multi-dimensional problems and to unstructured meshes. For example, Barth and Fredrickson[12,13] developed a high-order finite-volume approach for unstructured mesh based on k-exact least-squares reconstruction and Cockburn *et al.*[14–16] have formulated a family of high-order schemes for conservation laws referred to as discontinuous Galerkin (DG) methods. More recently, Ollivier-Gooch[17,18] has developed a data-dependent weighted least-squares reconstruction procedure, that uses a fixed stencil and seeks to enforce monotonicity of the scheme by introducing data-dependent weights for each point in the stencil. In addition, Wang *et al.*[19,20] and Liu *et al.*[21] have recently proposed variants of the DG method, referred to as spectral volume (SV) and spectral difference (SD) methods, for obtaining high-order solutions to hyperbolic conservation equations. More recently, extensions of these methods to viscous flows have been considered by Sun *et al.*[22] for the SV approach and by May and Jameson[23,24] for the SD method. The latter have also applied their scheme in combination with AMR to the Navier-Stokes system of equations. Note also that Barad and Collela have proposed a fourth-order-accurate AMR scheme for Poisson's equation.[25] Finally, De Rango and Zingg[26] have considered the application of high-order finite-difference methods to the prediction of turbulent aerodynamic flows. A recent summary of high-order schemes for the compressible Navier-Stokes equations is given by Venkatakrishnan *et al.*[27] Despite these advances in high-order accurate schemes for arbitrary meshes, there remains as yet no robust and effective way of providing high-order accuracy without degrading the solution monotonicity in the vicinity of discontinuities.

In the present work, a high-order central ENO (CENO) cell-centred finite-volume scheme is proposed for solving hyperbolic systems of conservation laws on body-fitted multi-block mesh in conjunction with a block-based adaptive mesh refinement technique. Use of this particular grid structure and AMR strategy has been shown to allow highly efficient and scalable parallel implementations of finite volume methods.[28] This proposed variant of the original ENO scheme is not based on either selecting or weighting reconstructions from multiple stencils. Instead, a hybrid solution reconstruction procedure is used that combines the unlimited high-order k-exact least-squares reconstruction technique of Barth[13] based on a fixed central stencil with a monotonicity preserving limited piecewise linear least-squares reconstruction algorithm.[13] Switching in the hybrid procedure is determined by a solution smoothness indicator that indicates whether or not the solution is resolved on the computational mesh. The limited reconstruction procedure is applied to computational cells with under-resolved solution content and the unlimited k-exact reconstruction scheme is used for cells

in which the solution is fully resolved. Due to cancellation of truncation errors, use of the central stencil will generally provide the most accurate reconstruction. This hybrid approach avoids the complexity associated with other ENO and WENO schemes that require reconstruction on multiple stencils which in some cases can produce poorly conditioned coefficient matrices. Additionally, the solution of the least-squares problem for the reconstruction is made more efficient with the use of a fixed stencil. For this reason, the hybrid CENO algorithm would seem very well suited for solution reconstruction on unstructured mesh. Another benefit of the CENO approach is that mesh adaptation can be directed based on the ability of the scheme to differentiate between resolved and under-resolved or non-smooth solution content. A novel h-refinement criterion based on the solution smoothness indicator is defined and used to control refinement of the body-fitted multi-block AMR mesh.

The CENO reconstruction leads to a finite-volume scheme for hyperbolic conservation equations that is uniformly accurate for smooth solutions (uniform accuracy is lost for non-smooth solutions), even near extrema and avoids the appearance of $O(1)$ numerical oscillations in under-resolved regions and for solutions containing strong discontinuities and/or shocks. Accuracy to any order is possible by simply expanding the support for the cell-centred reconstruction. Note that in earlier work, Harten and Chakravarthy[29] have proposed a technique to obtain an ENO reconstruction on a fixed central stencil by hybridizing the high-order reconstruction with a first-order formulation. The switching in their proposed hybrid central ENO scheme was based on undivided differences and the total variation diminishing (TVD) property[30] and not directly on the smoothness of the reconstructions. More recently, Haselbacher[10] has since explored the use of fixed stencil central reconstruction in the formulation of WENO schemes for unstructured mesh, but Haselbacher's approach is somewhat different to the current approach and schemes of accuracy higher than second order (piecewise linear reconstruction) were not formulated.

In what follows, a detailed summary of the proposed high-order CENO finite-volume scheme is provided, including discussions of the cell-centred finite-volume formulation, numerical flux evaluation using Riemann-solver based flux functions, hybrid CENO solution reconstruction, boundary condition prescription, and solution smoothness indicators for body-fitted multi-block quadrilateral meshes. The accuracy of the CENO reconstruction is then demonstrated for both smooth and non-smooth analytical functions. Additionally, the predictive capabilities of the proposed CENO finite-volume scheme is then demonstrated for both the one- and two-dimensional forms of the Euler equations of gas dynamics by comparing numerical solutions to analytic solutions for several problems, including Ringleb's flow, and by comparing the numerical predictions of the method to those of a standard second-order approach and the Harten's original ENO scheme for several flow problems. In addition, results obtained with the CENO scheme in conjunction with adaptive mesh refinement are also described to illustrate the predictive capabilities of the proposed high-order AMR scheme.

II. CENO Finite Volume Scheme

II.A. Hyperbolic Conservation Equations

The solution of hyperbolic systems of conservation laws of the form

$$\frac{\partial \mathbf{U}}{\partial t} + \vec{\nabla} \cdot \vec{\mathbf{F}} = 0\,, \tag{1}$$

will be considered here, where $\mathbf{U}$ is the conserved variable solution vector, $\vec{\mathbf{F}}$ is the solution flux dyad, and t is time. In particular, numerical solution of the one- and two-dimensional forms of the Euler equations of inviscid compressible gas dynamics will be discussed. For one space dimension, the Euler equations are given by

$$\frac{\partial \mathbf{U}}{\partial t} + \frac{\partial \mathbf{F}}{\partial x} = 0\,, \tag{2}$$

where $\mathbf{U}$ has the form

$$\mathbf{U} = \left[\begin{array}{ccc} \rho, & \rho u, & \rho e \end{array} \right]^{\mathrm{T}}, \tag{3}$$

x is the spatial coordinate, ρ is the gas density, u is the velocity of the gas, $e = p/(\rho(\gamma-1)) + u^2/2$ is the specific total energy, $p = \rho R T$ is the pressure, T is the gas temperature, R is the gas constant, γ is the specific heat ratio, and

$$\mathbf{F} = [\rho u, \rho u^2 + p, u(\rho e + p)]^{\mathrm{T}}\,, \tag{4}$$

is the solution flux vector. For a polytropic gas (thermally and calorically perfect gas), the ratio of specific heats, γ, is a constant and the specific heats are given by $C_v = R/(\gamma - 1)$ and $C_p = \gamma R/(\gamma - 1)$.

For two-dimensional planar flows, the Euler equations are as follows:

$$\frac{\partial \mathbf{U}}{\partial t} + \frac{\partial \mathbf{F}}{\partial x} + \frac{\partial \mathbf{G}}{\partial y} = 0\,, \tag{5}$$

where $\mathbf{U}$ is given by

$$\mathbf{U} = \left[\begin{array}{cccc} \rho, & \rho u, & \rho v, & \rho e \end{array} \right]^T\,, \tag{6}$$

x and y are the two spatial coordinates, u and v are the velocity components in the x- and y-coordinate directions, $e = p/(\rho(\gamma - 1)) + (u^2 + v^2)/2$, and

$$\mathbf{F} = [\rho u, \rho u^2 + p, \rho uv, u(\rho e + p)]^{\mathrm{T}}\,, \tag{7}$$

and

$$\mathbf{G} = [\rho v, \rho uv, \rho v^2 + p, v(\rho e + p)]^{\mathrm{T}}\,, \tag{8}$$

are the x- and y-direction solution flux vectors.

II.B. Semi-Discrete Form

High-order solutions of Eq. (1) are sought here in one- and two-space dimensions by applying a Godunov-type finite-volume spatial discretization procedure[31] in conjunction with high-order polynomial solution reconstruction and Riemann-solver based flux functions. The semi-discrete form of the finite-volume formulation applied to Eq. (1) for cell (i, j) of a two-dimensional multi-block mesh composed of quadrilateral computational cells is given by

$$\frac{d\mathbf{U}_{i,j}}{dt} = -\frac{1}{A_{i,j}} \sum_{l=1}^{N_f} \sum_{m=1}^{N_G} \left(\omega \vec{\mathbf{F}} \cdot \vec{n}\, \Delta\ell \right)_{i,j,l,m} = \mathbf{R}_{i,j}(\mathbf{U})\,, \tag{9}$$

where here each cell has $N_f = 4$ faces and a N_G-point Gaussian quadrature numerical integration procedure has been used to evaluate the solution flux through each face. The variable $\mathbf{U}_{i,j}$ is the conserved solution state for cell (i, j), $A_{i,j}$ is the area of the quadrilateral cell, ω is the quadrature weighting coefficient, and $\Delta\ell$ and $\vec{n}$ are the length of the cell face and unit vector normal to the cell face or edge, respectively. The vector, $\mathbf{R}_{i,j}$, is the residual vector.

II.C. Numerical Flux Evaluation

The numerical fluxes, $\vec{\mathbf{F}} \cdot \vec{\mathbf{n}}$, at the quadrature points, m, of faces, l, for each cell are determined from the solution of a Riemann problem. Given the left and right solution states, $\mathbf{U}_l$ and $\mathbf{U}_r$, at the quadrature points of the cell interfaces, the numerical flux is given by

$$\vec{\mathbf{F}} \cdot \vec{n} = \mathcal{F}(\mathbf{U}_l, \mathbf{U}_r, \vec{n})\,, \tag{10}$$

where the numerical flux $\mathcal{F}$ is evaluated by solving a Riemann problem in a direction defined by the normal to the face with initial data $\mathbf{U}_l$ and $\mathbf{U}_r$. In the present algorithm, both exact and approximate Riemann solvers can be used to solve the Riemann problem and evaluate the numerical flux. The Roe linearized Riemann solver,[32] HLLE and modified HLLE flux function due to Linde,[33–35] and the exact Riemann solver of Gottlieb and Groth[36] have all been implemented and may be used.

The left and right solution states, $\mathbf{U}_l$ and $\mathbf{U}_r$, are determined by performing piecewise k-order polynomial solution reconstruction within each computational cell. In the present work, a k-order CENO reconstruction scheme is proposed and used. Details of this approach are given in the next section.

Note that the spatial accuracy of the finite-volume scheme is obviously very dependent on the order of the solution reconstruction. For k-order reconstruction, a $k+1$-order accurate spatial discretization can be achieved for smooth problems. Note also that the number of Gauss quadrature points at which the numerical flux is evaluated is a function of the order of the solution reconstruction. Current practise is to use one quadrature point ($N_G = 1$) for second-order schemes (piecewise linear, $k = 1$, reconstruction) and two quadrature points ($N_G = 2$) for third- and fourth-order schemes (piecewise quadratic, $k = 2$, and cubic, $k = 3$ reconstruction) to ensure that the order of accuracy of the schemes is preserved.

II.D. Time-Marching Schemes

For all the test cases considered in this work, multi-stage explicit time-marching schemes have been used to solve the system of ordinary differential equations given by Eq. (9). For time accurate problems, either a two- or four-stage standard Runge-Kutta scheme is used, depending on the accuracy of the spatial reconstruction.

III. CENO Reconstruction

A high-order central ENO method is used for performing the piecewise k-order polynomial reconstruction within each of the computational cells. This variant of the original ENO scheme is not based on either selecting or weighting reconstructions from multiple stencils. Instead, a hybrid solution reconstruction procedure is used that combines the high-order k-exact least-squares reconstruction technique of Barth[13] based on a fixed central stencil with a monotonicity preserving limited piecewise linear least-squares reconstruction algorithm.[13] Switching in the hybrid procedure is determined by a solution smoothness indicator that indicates whether or not the solution is resolved on the computational mesh. The limited reconstruction procedure is applied to computational cells with under-resolved solution content and the unlimited k-exact reconstruction scheme is used for cells in which the solution is fully resolved.

III.A. k-Exact Reconstruction

In piecewise k-exact polynomial reconstruction, it is assumed that a solution variable, u, at any location, $\vec{r}$, in computational cell (i,j) has the form

$$u_{i,j}^{k}(\vec{r}) = \sum_{p_1=0}^{N_1} \sum_{p_2=0}^{N_2} (x-\bar{x}_{i,j})^{p_1} \, (y-\bar{y}_{i,j})^{p_2} \, D_{p_1 p_2}^{k} \tag{11}$$

where (x,y) are the Cartesian coordinates of the point of interest, $(\bar{x}_{i,j}, \bar{y}_{i,j})$ are the coordinates of the cell centroid, k is the order of the piecewise polynomial interpolant, the upper bounds for the indices p_1 and p_2 must satisfy the condition that $N_1 + N_2 \leq k$, and $D_{p_1 p_2}^{k}$ are the coefficients of the polynomial approximation to be determined. The latter are in general functions of the mean or average value solution, $\bar{u}_{i,j}$, within the cell and its neighbours. When determining the coefficients $D_{p_1 p_2}^{k}$, it is required that the following conditions be satisfied by the reconstruction procedure: i) the solution reconstruction must reproduce exactly polynomials of degree $N \leq k$; ii) the solution reconstruction must preserve the mean or average value within the computational cell; and iii) the reconstruction procedure must have compact support. The second condition implies that $\bar{u}_{i,j} = (1/A_{i,j}) \iint_{A_{i,j}} u_{i,j}^{k}(\vec{r}) dx dy$. The third condition involves the number and locality of the neighbouring solution states used in the cell reconstruction. The minimum size of the compact stencil is determined by the number of required unknown coefficients, but in practise, additional neighbours are included in order to make the reconstruction more robust in the presence of stretched meshes and solution gradients not aligned with the mesh. For body-fitted quadrilateral mesh, the current k-exact reconstruction scheme uses a fixed central stencil which includes 8 neighbour cells for $k = 1$ and 24 neighbours for $k = 2$, $k = 3$ and $k = 4$.

The evaluation of the coefficients $D_{p_1 p_2}^{k}$ requires the least-squares solution of an overdetermined system of linear equations $\mathbf{A}\,\mathbf{x} = \mathbf{B}$, where the coefficient matrix $\mathbf{A}$ of the linear system depends only on the mesh geometry and can be partially calculated in a preprocessing step. The preservation of the average value within the cell is explicitly enforced by expressing the coefficient D_{00}^{k} as a function of the other unknowns. Both Householder QR factorization algorithm[37] and orthogonal decomposition by SVD method[37] can be used to solve the weighted least squares problem and determine the other coefficients, the latter being favored for the computation of the pseudo-inverse matrix $\mathbf{A}^{-1}$ as described below. Note that use of a fixed central stencil here avoids the complexities associated with ENO and WENO schemes that require reconstruction on multiple stencils as well as many of the difficulties associated with poorly conditioned coefficient matrices for the least squares problems. In addition, the use of a fixed stencil allows the pseudo-inverse matrix $\mathbf{A}^{-1}$ to be stored and reused at successive time steps as long as the computational grid is not modified. In particular, it was found that such a procedure can provide a computational speed-up by a factor of about 5 for high-order two-dimensional Euler computations compared with the situation in which the coefficient matrix $\mathbf{A}$ is formed and a least-squares subroutine is called for each spatial reconstruction. Although the procedure based on reusing the pseudo-inverse matrix requires extra storage, the additional memory requirements are

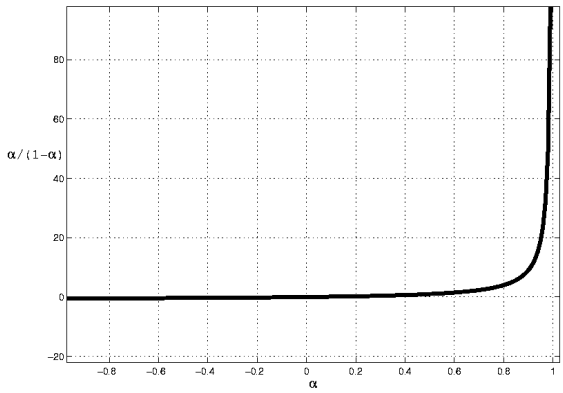

Figure 1. The graph of $f(\alpha) = \frac{\alpha}{(1-\alpha)}$.

not that substantial and are generally readily available on most modern distributed memory architectures. This procedure therefore represents a practical approach for reducing the cost of the proposed high-order reconstruction and is used here.

III.B. Smoothness Indicator

The proposed CENO scheme preserves solution monotonicity in regions of large gradients or discontinuities by reverting the high-order k-exact reconstruction to a limited piecewise linear ($k=1$) reconstruction. The slope limiters of Barth-Jesperson and Venkatakrishnan are used[13,38] in the limited reconstruction. In order to detect regions where the order of the reconstruction should be reduced and the limiters applied, a smoothness indicator is computed for every variable individually within each cell as part of a post-analysis step after the unlimited k-exact reconstruction has been performed. The smoothness indicator is then used in the manner described below to ensure that the limited linear reconstruction procedure is applied to computational cells with under-resolved and/or non-smooth solution content and the unlimited k-exact reconstruction scheme is where the solution is fully resolved.

The form of the smoothness indicator used here was inspired by the definition of multiple-correlation coefficients that are often used in evaluating the accuracy of curve fits.[37] The smoothness indicator, $\mathcal{S}$, is calculated in terms of a smoothness parameter, α, and information about the number of unknowns (degrees of freedom), DOF, and size of the stencil, SOS, used in the reconstruction. It is taken to have the form

$$\mathcal{S} = \frac{\alpha}{\max\left((1-\alpha),\epsilon\right)} \frac{(SOS - DOF)}{(DOF - 1)} \tag{12}$$

where α is determined as follows

$$\alpha = 1 - \frac{\sum_{\gamma}\sum_{\delta}\left(u^k_{\gamma,\delta}(\vec{\bar{r}}_{\gamma,\delta}) - u^k_{i,j}(\vec{\bar{r}}_{\gamma,\delta})\right)^2}{\sum_{\gamma}\sum_{\delta}\left(u^k_{\gamma,\delta}(\vec{\bar{r}}_{\gamma,\delta}) - \bar{u}_{i,j}\right)^2} \tag{13}$$

and where the ranges of the indices, γ and δ, are taken to include all control volumes in the reconstruction stencil for cell (i,j), $\vec{\bar{r}}_{\gamma,\delta}$ is the centroid of the cell (γ,δ), and the tolerance, ϵ, has been introduced in order to avoid division by zero. A suitable value for ϵ is 10^{-8}. It should be evident that the parameter α compares the values of the reconstructed solution at the centroids of neighbouring cells used in the solution reconstruction for cell (i,j). The range for α is $-\infty < \alpha \leq 1$ and it will approach unity as the solution becomes smooth and near perfect reconstruction is achieved. The variation of $\frac{\alpha}{(1-\alpha)}$ is depicted in Fig. 1 and the figure shows that $\mathcal{S}$ rapidly becomes large as α approaches unity.

The smoothness indicator, $\mathcal{S}$, is then compared to a pass/no-pass cutoff value, $\mathcal{S}_c$. The cutoff was determined from a wide range of numerical experiments and values for $\mathcal{S}_c$ in the range 2,500-5,000 seem to work well. It should be pointed out that smoothness indicators for smooth solutions are typically orders of magnitude larger than the range of cutoff values (e.g. 100,000). Thus for $\mathcal{S} < \mathcal{S}_c$, the solution is deemed to

be under-resolved and/or non-smooth and the high-order k-exact reconstruction is replaced by limited linear reconstruction in that cell. For $\mathcal{S} > \mathcal{S}_c$, the unlimited high-order reconstruction is deemed to be acceptable and retained.

III.C. Reconstruction at the Boundaries

Correct high-order treatment of boundary conditions is crucial for developing accurate numerical schemes. It is especially important for high-order methods, where errors due to geometrical approximation may dominate the discretization error, mitigating the full capabilities of a high-order scheme. One approach to imposing high-order boundary conditions is to make use of extra rows of ghost cells which are added beyond the geometric boundary of the computational domain. Solution states are then imposed in the ghost cells in such a way that the reconstructed solution and/or flux at the boundary flux interior cell approximates those associated with the particular boundary condition. An alternative approach is to enforce the boundary conditions by constraining the least-squares reconstruction in control volumes adjacent to the boundary as described by Olivier-Gooch and Van Altena.[39] In the current work, both procedures (i.e., ghost cells and constrained reconstruction) for boundary condition prescription have been implemented. In order to obtain high-order accuracy at boundaries, the geometric data (i.e., cell area, centroid, geometric moments, normals, edge lengths, locations of the Gauss quadrature integration points) are computed to the same order of accuracy as that of the interior scheme. In order to solve the enlarged system of equations arising from the constrained least squares reconstruction (boundary constraints plus reconstruction conditions), Gauss elimination with pivoting is used to eliminate the rows associated with the boundary condition constraints, and the remaining least-squares problem is again solved using Householder QR factorization.

IV. Adaptive Mesh Refinement

A flexible block-based hierarchical data structure is used in conjunction with the CENO finite-volume scheme described above to facilitate automatic solution-directed mesh adaptation on body-fitted multi-block quadrilateral mesh. The method allows for anisotropic mesh refinement and is well suited to parallel implementation via domain decomposition. Aspects of the block-based AMR algorithm for multi-block quadrilateral mesh are described in the recent work by Sachdev *et al.*[28] and the approach has been successfully applied to the prediction of laminar and turbulent diffusion flames,[40,41] micron-scale flows,[42] and multi-phase rocket motor core flows.[28]

As described above, the solution of the conservation equations by the CENO finite-volume method of the preceding section provides area-averaged solution quantities within quadrilateral computational cells and these cells are embedded in structured blocks consisting of $N_{\text{cells}} = N_x \times N_y$ cells, where N_x and N_y are even, but not necessarily equal integer values. Solution data associated with each block are stored in indexed array data structures and it is therefore straightforward to obtain solution information from neighbouring cells within blocks. Mesh adaptation is accomplished by the dividing and coarsening of appropriate solution blocks. In regions requiring increased cell resolution, a "parent" block is refined by dividing itself into four "children" or "offspring" (see Fig. 2b). Each of the four quadrants or sectors of a parent block becomes a new block having the same number of cells as the parent and thereby doubling the cell resolution in the region of interest. This process can be reversed in regions that are deemed over-resolved and four children are coarsened into a single parent block. The mesh refinement is constrained such that the grid resolution changes by only a factor of two between adjacent blocks and the minimum resolution is not less than that of the initial mesh. The hybrid CENO solution reconstruction procedure is used in conjunction with standard multi-grid-type restriction and prolongation operators to evaluate the solution on all blocks created by the coarsening and division processes, respectively.

In previous work, the coarsening and division of blocks was directed using multiple physics-based refinement criteria.[28,40–42] In this work, an h-refinement criterion based on the solution smoothness indicator is defined and used to control refinement of the body-fitted multi-block AMR mesh. The form considered herein for the CENO-based refinement criterion is:

$$\mathcal{R}_c = e^{-\frac{\max(0,\mathcal{S})}{\mathcal{U}_s * \mathcal{S}_c}} \tag{14}$$

where $\mathcal{U}_s$ is a scaling coefficient. Based on the range of $\mathcal{S}$ and the above definition for the refinement criterion, it should be evident that $\mathcal{R}_c$ always takes values in the range $(0, 1]$. Each block is then assigned the maximum

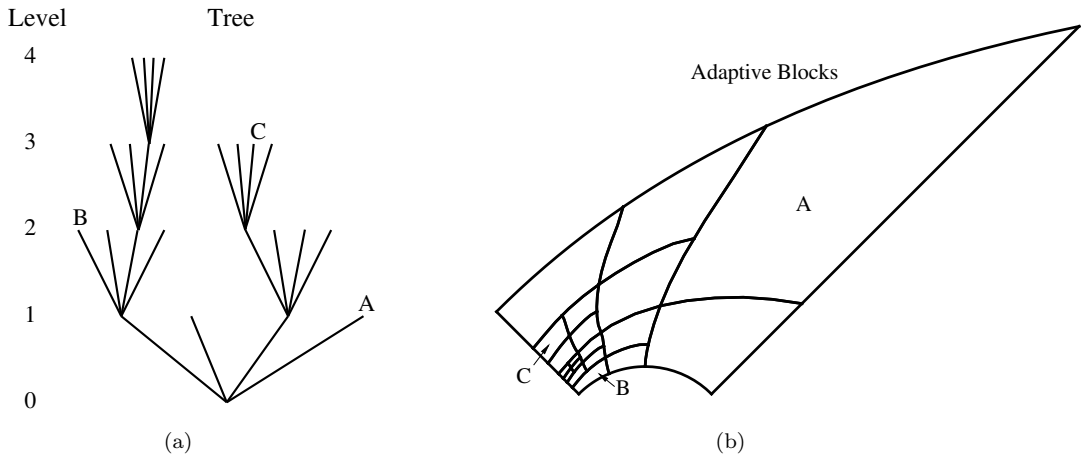

Figure 2. (a) Adaptive mesh refinement quad-tree data structure, and (b) associated solution blocks for a quadrilateral body-fitted mesh.

$\mathcal{R}_c$ value of all cells within the block and in order to decide which blocks are to undergo mesh refinement, refining and coarsening thresholds are used. The coefficient, $\mathcal{U}_s$, is introduced for convenience and provides an easy way of adjusting the values of the coarsening and refining thresholds relative to the value of the cutoff $\mathcal{S}_c$.

In order that the finite-volume scheme can be applied to all blocks in a more independent manner, some solution information is shared between adjacent blocks having common interfaces. This information is stored in additional layers of overlapping "ghost" cells associated with each block. The number of ghost cells required depends on the accuracy of the scheme and ranges from two (for the second-order scheme) to three (for the fourth-order scheme). At interfaces between blocks of equal resolution, these ghost cells are simply assigned the solution values associated with the appropriate interior cells of the adjacent blocks. At resolution changes, restriction and prolongation operators, similar to those used in block coarsening and division, are employed to evaluate the ghost cell solution values. Within the AMR approach, additional inter-block communication is also required at interfaces with resolution changes to strictly enforce the flux conservation properties of the finite-volume scheme.[43,44] In particular, the interface fluxes computed on more refined blocks are used to correct the interface fluxes computed on coarser neighbouring blocks and ensure the solution fluxes are conserved across block interfaces.

A hierarchical tree-like data structure with multiple "roots", multiple "trees", and additional interconnects between the "leaves" of the trees is used to keep track of mesh refinement and the connectivity between solution blocks (see Fig. 2a). The blocks of the initial mesh are the roots of the forest which are stored in an indexed array data structure. Associated with each root is a separate "quadtree" data structure that contains all of the blocks making up the leaves of the tree created from the original parent blocks during mesh refinement. Each grid block corresponds to a node of the tree. Traversal of the multi-tree structure by recursively visiting the parents and children of solution blocks can be used to determine block connectivity. However, in order to reduce overhead associated with accessing solution information from adjacent blocks, the neighbours of each block are computed and stored, providing direct interconnects between blocks in the hierarchical data structure that are neighbours in physical space. One of the advantages of the hierarchical quadtree data structure is that it readily permits local mesh refinement. Local modifications to the multi-block mesh can be performed without re-gridding the entire mesh and re-calculating all solution block connectivities.

Although the block-based AMR approach described above is somewhat less flexible and incurs some inefficiencies in solution resolution as compared to a cell-based approaches (i.e., for the same solution accuracy, generally more computational cells are introduced in the adapted grid), the block-based method offers many advantages over cell-based techniques when parallel implementation of the solution algorithm is considered and computational performance issues are taken into account. In particular, the multi-block quadrilateral mesh and quadtree data structure lends itself naturally to domain decomposition and thereby should

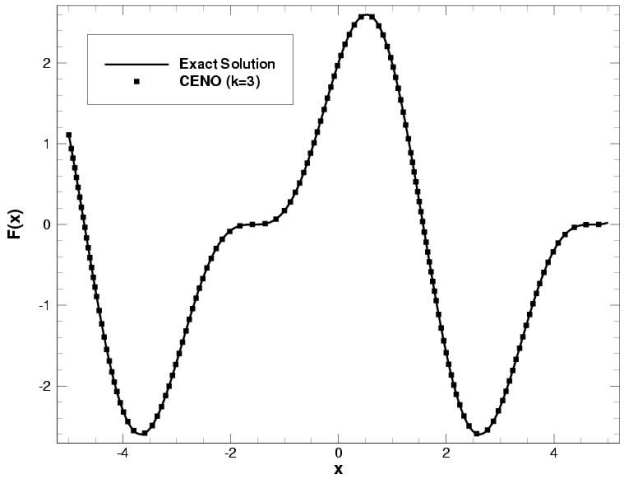

Figure 3. Piecewise cubic ($k = 3$) hybrid CENO reconstruction of the smooth trigonometric function $f(x) = \sin(2x) + 2\cos(x)$ on a one-dimensional uniform mesh of 32 computational cells is compared to the exact function for $-5 < x < 5$.

enable efficient and scalable implementations of the CENO finite-volume scheme on distributed-memory multi-processor architectures.[28, 40–42]

V. Numerical Results

Numerical results are now described for solution reconstruction in one- and two-space dimensions, as well as for various one- and two-dimensional flow problems governed by the Euler equations. Results for both fixed and AMR mesh are described.

V.A. One-Dimensional Reconstruction on Fixed Mesh

To assess the accuracy of the hybrid CENO scheme, reconstructions of the smooth trigonometric function $f(x) = \sin(2x)+2\cos(x)$ on cell-centred one-dimensional uniform meshes are compared to the exact solution. In Fig. 3, the cubic ($k = 3$) reconstruction obtained with 32 computational cells for $-5 < x < 5$ is shown together with the exact function. It can be seen in the figure that this smooth function features multiple extrema and inflection points which can be accurately captured only with polynomials of appropriate order. Low-order methods cannot properly resolve such solution features.

The L_1, L_2, and L_∞ norms of the reconstruction error associated with hybrid CENO reconstruction are shown in Fig. 4a and Fig. 4b. Results are given for piecewise linear ($k = 1$), quadratic ($k = 2$), cubic ($k=3$), and quartic ($k=4$) reconstruction and compared to reconstruction errors obtained using the original ENO scheme of Harten *et al.*[3] It is evident that the reconstruction errors of the CENO scheme are quite comparable to those of the ENO approach, and the expected theoretical asymptotic convergence rates of the 2nd-, 3rd-, 4th-, and 5th-order accurate methods are achieved (the order of accuracy of k-exact CENO schemes is $k + 1$ for smooth resolved functions).

A similar set of numerical results are shown in Fig. 5b for the reconstruction of the smooth function $f(x) = e^{-4x}\sin(5x)$ on $-5 < x < 5$. Results are depicted for cubic ($k=3$) and quartic ($k=4$) CENO reconstructions and compared to ENO reconstructions. This function features a very large peak near $x = -4.5$ (refer to Fig. 5a). The proposed CENO scheme is able to handle this feature in both an accurate and robust manner. For meshes containing less than 40-50 cells, the function is under-resolved and monotonic piecewise linear reconstruction of the peak is obtained. As more cells are added, the function is then resolvable on the mesh and a smooth 4th-order reconstruction of the function is achieved with the expected asymptotic convergence rate of this 5th-order accurate scheme. Again, the reconstruction errors of the CENO scheme are very comparable to those of the ENO approach.

The robustness of the CENO approach is now illustrated by considering the reconstruction of a discontinuous step function on a one-dimensional uniform mesh for $-1 < x < 4$ containing 11 computational cells. Results obtained using piecewise linear ($k=1$), quadratic ($k=2$), cubic ($k=3$), and quartic ($k=4$) ENO and

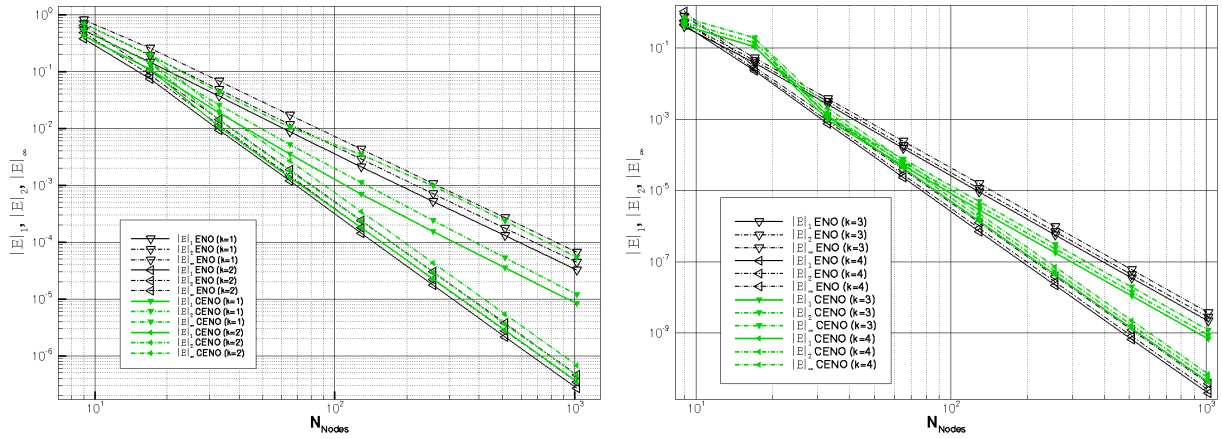

(a) (b)

Figure 4. L_1, L_2, and L_∞ **norms of the reconstruction errors for ENO and hybrid CENO reconstructions of the function shown in Fig. 3 as a function of the number of computational cells. (a) Piecewise linear** ($k=1$) **and quadratic** ($k=2$) **reconstructions and (b) piecewise cubic** ($k=3$) **and quartic** ($k=4$) **reconstructions are shown.**

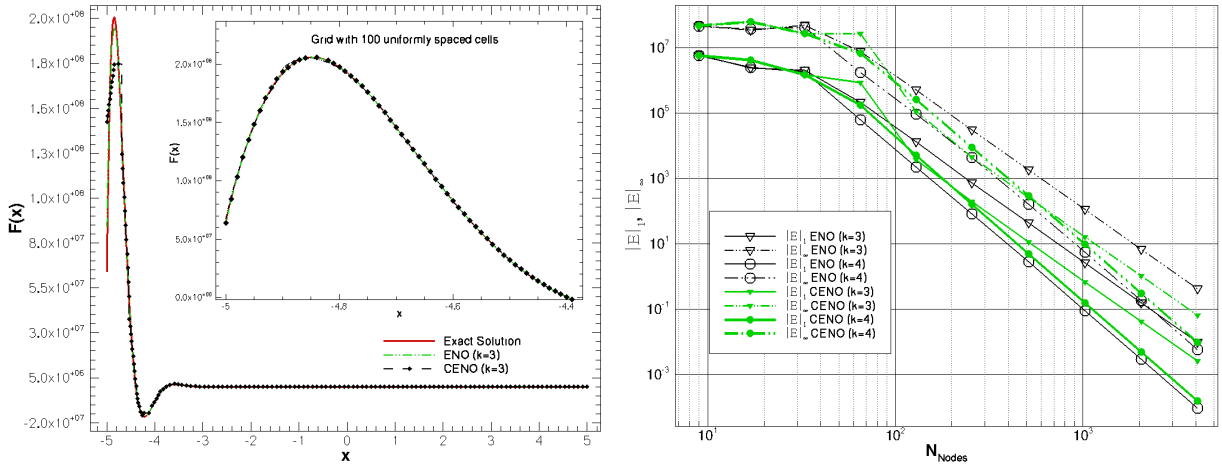

(a) (b)

Figure 5. (a) Reconstruction of $f(x) = e^{-4x}\sin(5x)$ **on cell-centred one-dimensional uniform mesh for** $-5 < x < 5$ **containing 64 and 100 computational cells. Results obtained using piecewise cubic** ($k=3$) **ENO and hybrid CENO schemes are compared to the exact function; and (b)** L_1 **and** L_∞ **norms of the reconstruction errors for ENO and hybrid CENO reconstructions of this function versus the number of computational cells (piecewise cubic** ($k=3$) **and quartic** ($k=4$) **reconstructions are shown).**

hybrid CENO schemes are compared to a piecewise constant representation and the exact function (refer to Fig. 6). It is quite evident that the discontinuous solution is not resolvable on any mesh and the hybrid CENO scheme is able to recognize this and reverts to a monotonic piecewise linear representation of the solution.

V.B. Two-Dimensional Reconstruction on Fixed Mesh

The reconstruction of a non-smooth function in two dimensions by the proposed hybrid CENO scheme is considered next. Reconstruction of the function examined in previous studies by Abgrall[4] and Ollivier-Gooch[18] is considered. A contour plot of Abgrall's function is given in Fig. 7a. A similar contour plot of a fourth-order ($k=4$) CENO reconstructed solution of this function for a stretched 80×80 non-uniform mesh is given in Fig. 7b and cross sections of the reconstructed solutions using the 2nd-order ($k=2$), 3rd-order ($k=3$), and 4th-order ($k=4$) CENO schemes for the 80×80 non-uniform mesh are depicted in Fig. 7c and compared to the exact representation of the function as well as those for simple piecewise constant

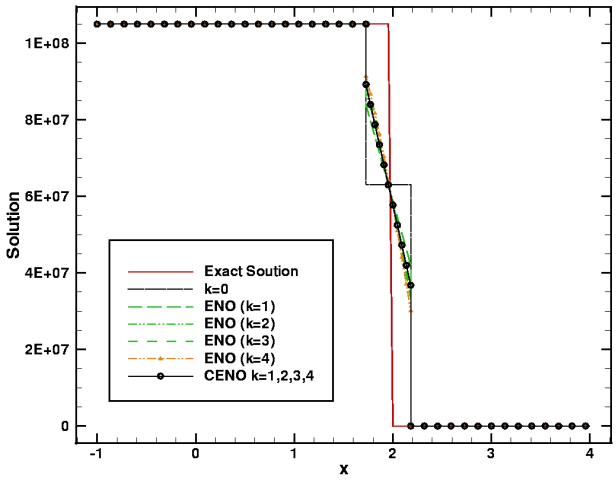

Figure 6. Reconstruction of a discontinuous step function on a one-dimensional uniform mesh for $-1 < x < 4$ containing 11 computational cells. Results obtained using piecewise quadratic ($k=2$), cubic ($k=3$), and quartic ($k=4$) ENO and hybrid CENO schemes are compared to a piecewise constant representation and the exact function.

reconstruction. It is evident that the CENO reconstruction accurately represents the Abgrall's function in smooth regions while providing virtually non-oscillatory reconstructions near discontinuities.

V.C. One-Dimensional Euler Equations on Fixed Mesh

The application of the proposed high-order CENO finite-volume scheme to the numerical solution of a hyperbolic system of nonlinear conservation laws has also been investigated. Here, numerical solutions of the one-dimensional form of the Euler equations of compressible gas dynamics are considered for the blast wave interaction problem of Woodward and Colella.[45] Numerical results for this case are shown in Fig. 8 for both the 4th-order CENO scheme with $k=3$ hybrid reconstruction and a 4th-order version of the original ENO scheme using locally defined characteristic variables. Results for a 2nd-order TVD scheme with limited linear piecewise linear reconstruction are also depicted in the figure. A uniform mesh containing 400 cells was used. The "exact solution" was generated with the 4th-order ENO algorithm on a mesh with 800 cells. It can be seen that the predictions of the CENO scheme are very similar to those of the ENO method, and both yield significantly improved results as compared to the TVD scheme for this very challenging problem involving strong nonlinear wave interactions.

V.D. Two-Dimensional Euler Equations on Fixed Mesh

The application of the proposed high-order CENO finite-volume scheme to the solution of the two-dimensional form of the Euler equations using body-fitted multi-block quadrilateral mesh has also been considered herein. The accuracy of the high-order spatial discretization scheme is demonstrated by first considering numerical predictions of Ringleb's flow. Ringleb's flow involves isentropic, expanding, irrotational flow between two streamlines and exact solutions for this smooth continuous flow field can be determined by analytical means.[46] As a first case, an entirely subsonic flow solution is considered for which the domain is defined by streamlines corresponding to $k_{min} = 0.4$ and $k_{max} = 1.0$ and by the subsonic inflow boundary corresponding to $q = 0.3$. In this case, inflow, outflow, and streamline boundary conditions based on the exact solution are prescribed. The predicted Mach number distribution for subsonic Ringleb's flow obtained using the 4th-order CENO finite-volume scheme on a 40×40 body-fitted mesh is shown in Fig. 9a. The L_1, L_2, and L_∞ norms of the error in the predicted solution density for 3rd- and 4th-order versions ($k=2$ and $k=3$) of the proposed CENO finite-volume scheme obtained on a series of grids ranging in size from 10×10 to 160×160 is given in Fig. 9b for this subsonic flow. As the mesh is refined, the slopes of the L_1- and L_2-norms for the 3rd- and 4th-order schemes approach -3.02, -3.05, -4.13, and -4.05, respectively, indicating that the expected theoretical accuracy has been achieved in each case.

A transonic variant of Ringleb's flow defined by $k_{min} = 0.5$, $k_{max} = 1.2$, and $q = 0.3$ has also been examined here. In this case, reflection boundary conditions were applied along the streamline boundaries

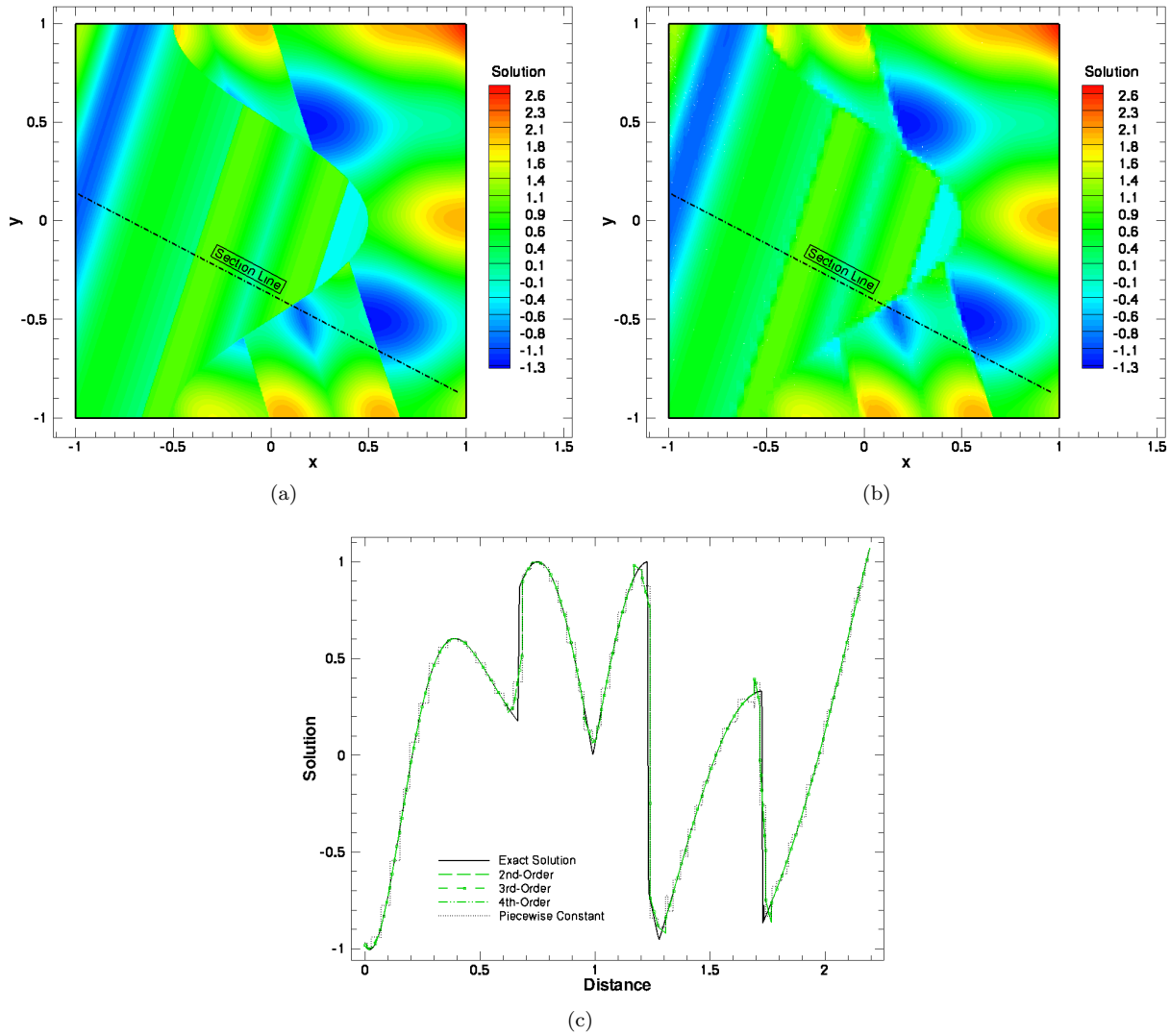

Figure 7. (a) The exact solution of the non-smooth two-dimensional function of Abgrall;[4] (b) contours of a fourth-order ($k=4$) CENO reconstructed solution of the Abgrall function for a stretched 80×80 non-uniform mesh; and (c) cross sections of 2nd-order ($k=2$), 3rd-order ($k=3$), and 4th-order ($k=4$) CENO reconstructed solution of the Abgrall function along the line shown in (a) and (b) above.

by enforcing the inviscid (slip) condition, $\vec{V}\cdot\vec{n}=0$, at all Gauss integration points via the constrained least-squares reconstruction procedure outline above. The predicted Mach number distribution for subsonic Ringleb's flow obtained using the 4th-order CENO finite-volume scheme on a 80×80 body-fitted mesh is given in Fig. 10a and the L_1, L_2, and L_∞ norms of the error obtained using the 3rd- and 4th-order versions of the CENO scheme are shown in Fig. 10b. In this case, the slopes of the L_1- and L_2-norms for the 3rd- and 4th-order CENO schemes approach -3.04, -2.97, -3.99 and -3.74, respectively, illustrating that the accuracy of the scheme can be maintained at curved boundaries by using constrained least-squares reconstruction and accurate boundary representation.

The accuracy and performance of the proposed CENO schemes are now further examined by considering subsonic flow past a circular cylinder with a freestream Mach number of $M_\infty = 0.38$. The predicted Mach number distributions obtained using the 2nd- and 4th-order CENO schemes are given in Figs. 11a and 11b, respectively. It is quite noticeable that, for the same mesh resolution, the 4th-order CENO solution is significantly more accurate than the 2nd-order CENO one. To quantify these findings, the L_2 norms of the error in the predicted entropy (the flow is homentropic and the entropy is constant) are determined on a sequence of four structured O-grids ranging in size from 20×10 to 160×80 and shown in Fig. 12. As the

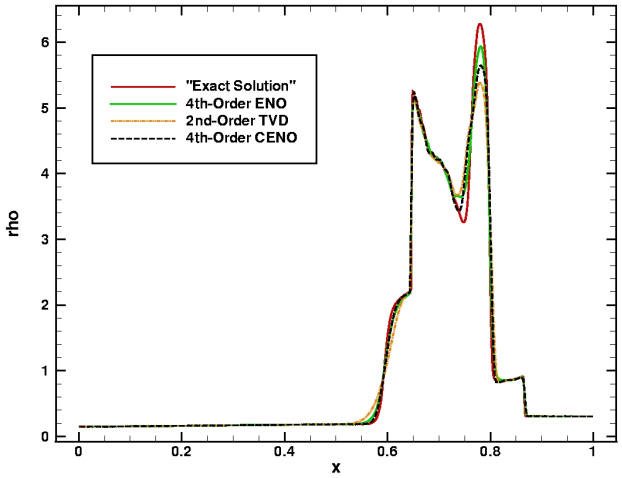

Figure 8. Numerical solutions of the one-dimensional blast wave interaction problem of Woodward and Colella.[45] Predictions of flow density obtained using the 4th-order CENO finite-volume scheme are depicted and compared to solutions obtained using a 4th-order ENO scheme and a 2nd-order TVD scheme with limited linear piecewise linear reconstruction for a uniform mesh with 400 cells.

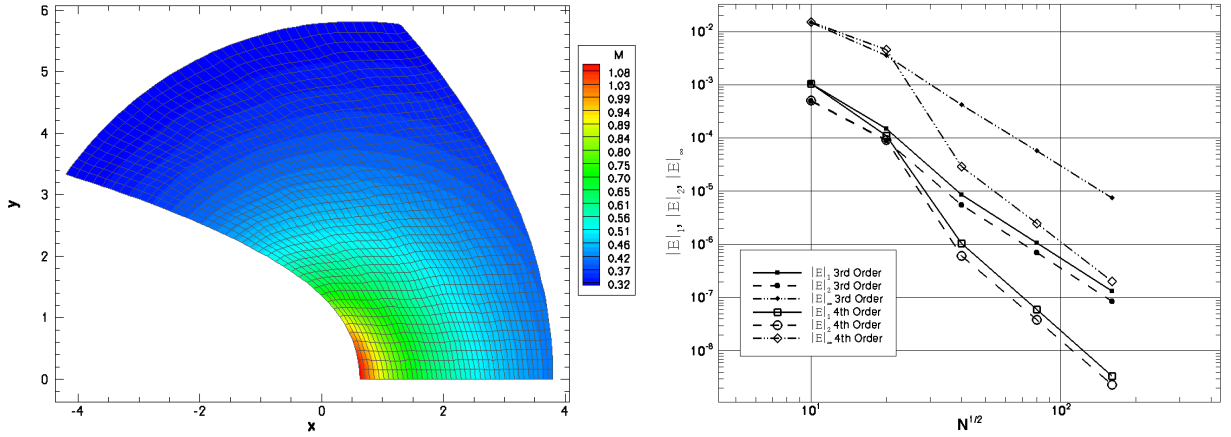

(a) (b)

Figure 9. (a) Predicted Mach number distribution for subsonic Ringleb's flow obtained using the 4th-order CENO finite-volume scheme; and (b) L_1, L_2, and L_∞ norms of the error in the predicted solution density for subsonic Ringleb's flow obtained using the 3rd- and 4th-order versions of the CENO scheme as a function of mesh density.

mesh is refined, the slopes of the L_2-norms for the 3rd- and 4th-order schemes approach -2.74 and -4.02, respectively.

To demonstrate the ability of the CENO schemes to handle robustly flows with both smooth and non-smooth regions, the predicted Mach number distribution obtained on a 160×160 grid $M = 1.5$ flow past a circular cylinder is shown in Fig. 13a. By reducing to limited linear reconstruction near the shocks in the flow, a monotone solution is obtained using the 4th-order scheme. The regions of the flow in which the CENO scheme uses the unlimited cubic and limited linear reconstruction procedures are shown in Fig. 13b.

Finally, the periodic linear advection of density variation is considered here in a rectangular box in order to assess the computational cost of the 4th-order CENO scheme versus that of a limited 2nd-order method. Since the computational work associated with each of the two schemes is definitely problem dependent and involves other parameters too, such as the accuracy of boundary conditions, the time marching method or the grid topology, a full comparison between the two methods would require a more elaborated study than the present one. However, the model problem chosen for this test case is still relevant for providing useful insight into the computational costs of the high-order CENO schemes as compared to a standard 2nd-order method. In Fig. 14a the exact representation of the chosen density variation is shown, which is given by $\rho(x, y) = 1.0 + 0.5 \cos(3\,\mathcal{T}(x)) \sin(5\,\pi\,\mathcal{T}(x))$, where $\mathcal{T}(x)$ represents a linear mapping of the

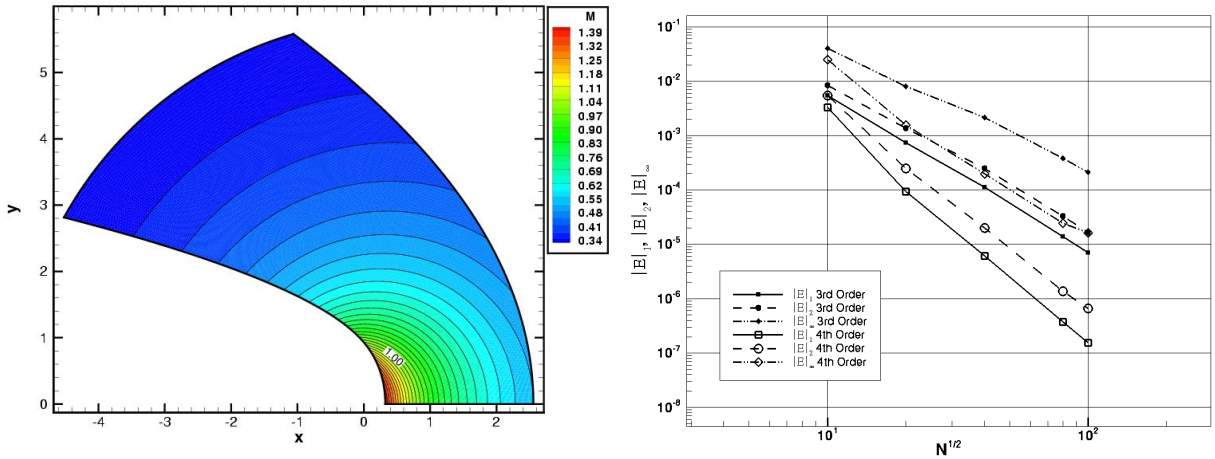

(a) (b)

Figure 10. (a) Predicted Mach number distribution for transonic Ringleb's flow obtained using 4th-order CENO finite-volume scheme; and (b) L_1, L_2, and L_∞ norms of the error in the predicted solution density for transonic Ringleb's flow obtained using the 3rd- and 4th-order versions of the CENO scheme as a function of mesh density.

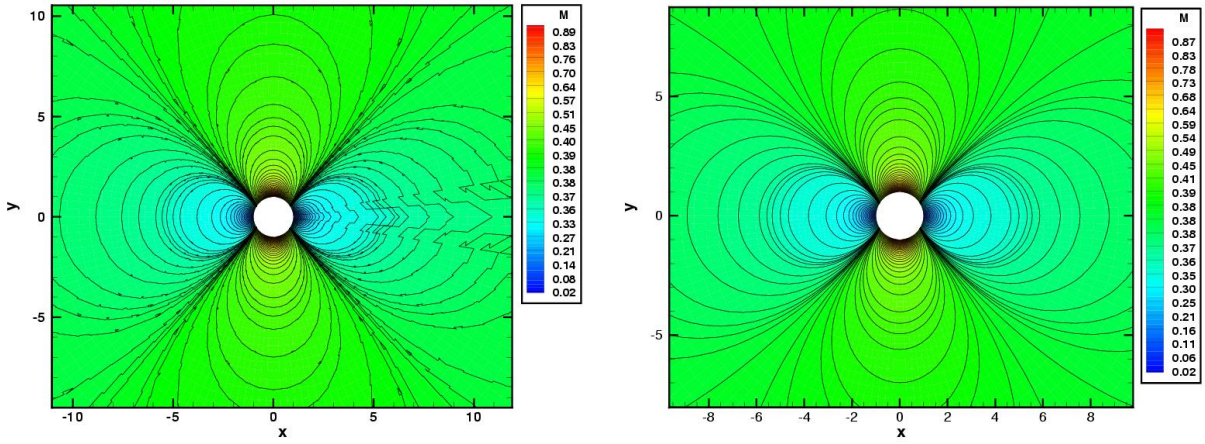

(a) (b)

Figure 11. (a) Predicted Mach number distributions for $M=0.38$ subsonic flow past a circular cylinder obtained using the 2nd-order CENO on a 80×40 grid; and (b) predicted Mach number distributions for $M=0.38$ subsonic flow past a circular cylinder obtained using the 4th-order CENO on the same computational grid used to obtain (a).

domain $[-100, 100]$ into the domain $[-1, 1]$. The predicted density solution obtained after one full period for this problem using the 4th-order CENO scheme on a Cartesian grid with 200×20 computational cells is shown in Fig. 14b. A visual comparison between the two density variations shown in Fig. 14 reveals that the cubic interpolant used by the high-order k-exact reconstruction captures all the inflection points of this smooth density variation very well and the solution is being recognized everywhere as smooth by the CENO approach. The error norms as well as the simulation CPU time and memory requirements corresponding to the limited 2nd-order and the 4th-order CENO schemes are presented in Table 1. Based on the data shown in the table it can be seen that for the same mesh resolution the current 4th-order CENO scheme requires about 10 times more computational work than the 2nd-order method and about 1.5 times more memory. However, in order to obtain the same accuracy provided by the 4th-order CENO, a limited 2nd-order scheme would require about 20 times more computational cells (e.g. 80,000 instead of 4,000) which, in turn, necessitate approximately 47 times more computational work than the one of the high-order CENO. As a further benefit, this large saving on the number of computational cells is translated into a decrease in the memory requirements by a factor of about 6.5, which shows the potential benefits of the high-order

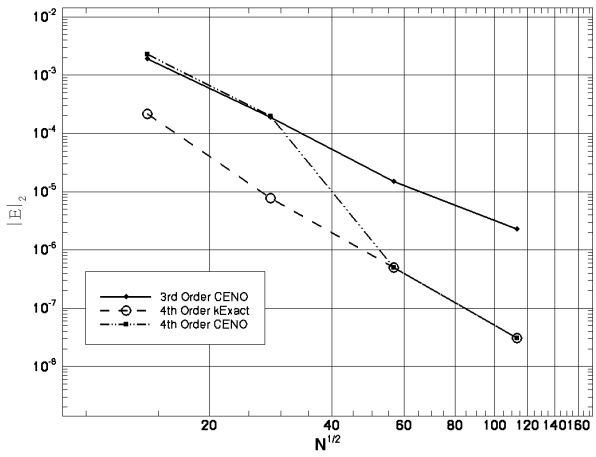

Figure 12. L_2 **norms of the error in entropy for** $M = 0.38$ **flow past a circular cylinder.**

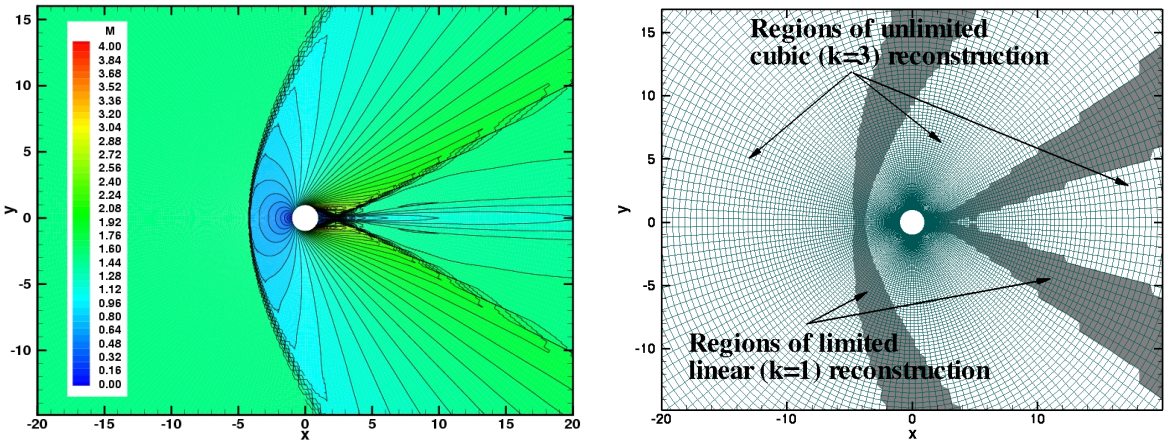

(a) (b)

Figure 13. (a) Predicted Mach number distribution for $M = 1.5$ **flow past a circular cylinder obtained using the 4th-order CENO scheme on a** 160×160 **grid; and (b) regions in which the CENO scheme uses unlimited cubic and limited linear reconstruction for** $M = 1.5$ **flow past a circular cylinder.**

method.

V.E. Two-Dimensional Reconstruction with AMR

Reconstruction of Abgrall's function[4] is now re-considered in conjunction with AMR. A contour plot of a third-order ($k = 3$) CENO reconstructed solution of this function on an initial uniform 10×10 Cartesian mesh consisting of 1 block and 100 computational cells is shown in Fig. 15a. The initial 10×10 mesh is given in Fig. 16a. A sequence of refined mesh is then generated using the h-refinement criterion defined above. The Abgrall function is re-imposed on each mesh level before the mesh is further refined. A sequence of eight mesh refinements was carried out and the resulting multi-block AMR meshes are depicted in Fig. 16. The final mesh consisted of 3,535 blocks 10×10 and 353,500 cells with a refinement efficiency of $\eta = 0.946$. The reconstructed solution on the finest mesh using the 4th-order CENO scheme is shown in Fig. 15b. A cross section of the cubic CENO reconstructed solution along the section line shown in Fig. 15b is depicted in Fig. 15c and compared to the exact representation of the Abgrall function. In addition, the regions in which the hybrid CENO scheme uses the unlimited cubic and limited linear reconstruction procedures are shown in Fig. 15d. It can be seen that the regions where limited piecewise reconstruction is used correspond to regions where Abgrall's function is either not $\mathcal{C}^0$ or not $\mathcal{C}^1$ continuous. The refinement of the AMR mesh is automatically directed toward these regions. Another important observation is that the proposed h-refinement criterion is capable of identifying all of the discontinuous regions, regardless of the strength of

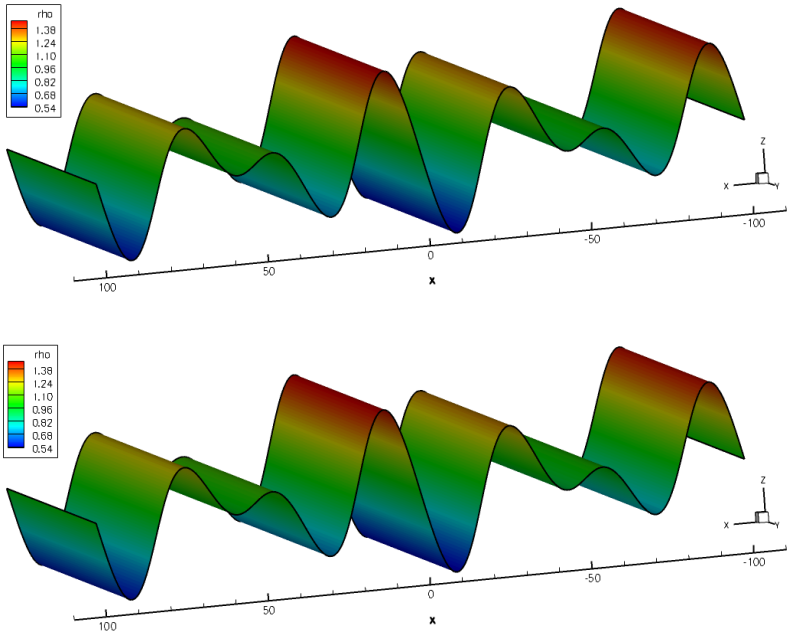

Figure 14. (a) Exact solution for the periodic linear advection of the density variation $\rho(x, y) = 1.0 + 0.5 \cos(3\ \mathcal{T}(x)) \sin(5\ \pi\ \mathcal{T}(x))$; and (b) Predicted density distribution for the advection of density variation shown in (a) after one full period using the 4th-order CENO scheme on a 200×20 Cartesian grid.

Table 1. Error norms, simulation CPU time and memory requirements associated with the limited 2nd-order and the 4th-order CENO schemes obtained for the periodic linear advection of the density variation shown in Fig. 14.

# Cells	$\mathcal{O}(\Delta x^2)$		$\mathcal{O}(\Delta x^4)$	
4,000 (200x20)	$L1$:	2.68E-02	$L1$:	1.85E-04
	$L2$:	3.26E-02	$L2$:	2.18E-04
	$LMax$:	7.36E-02	$LMax$:	9.46E-04
	$Time(h)$:	0:01:20	$Time(h)$:	**0:10:38**
	$Mem(kB)$:	20,336	$Mem(kB)$:	**31,232**
8,000 (400x20)	$L1$:	9.38E-03	$L1$:	1.32E-05
	$L2$:	1.16E-02	$L2$:	2.02E-05
	$LMax$:	2.98E-02	$LMax$:	2.11E-04
	$Time(h)$:	0:04:18	$Time(h)$:	0:41:03
	$Mem(kB)$:	30,000	$Mem(kB)$:	50,816
80,000 (4000x20)	$L1$:	1.10E-04	$L1$:	-
	$L2$:	2.20E-04	$L2$:	-
	$LMax$:	1.33E-03	$LMax$:	-
	$Time(h)$:	**8:23:38**	$Time(h)$:	-
	$Mem(kB)$:	**203,680**	$Mem(kB)$:	-

the solution jumps.

V.F. Two-Dimensional Euler Equations with AMR

The application of the proposed high-order AMR CENO finite-volume scheme to the solution of supersonic flow past a circular cylinder is again considered. In this case the freestream Mach number is $M_\infty = 2.1$ and the capability of the high-order scheme is examined in conjunction with AMR. The predicted pressure distributions obtained using the 4th-order CENO scheme on a final mesh consisting of 2,150 blocks and 215,000 computational cells is shown in Fig. 17a. Corresponding to this solution, the regions of the flow in which the CENO scheme uses the unlimited cubic and limited linear reconstruction are shown in Fig. 17b. The sequence of adaptively refined meshes leading to the final refined mesh starting with an initial mesh that consists of 8 10×10 solution blocks is depicted in Fig. 18. The results clearly show that the proposed AMR

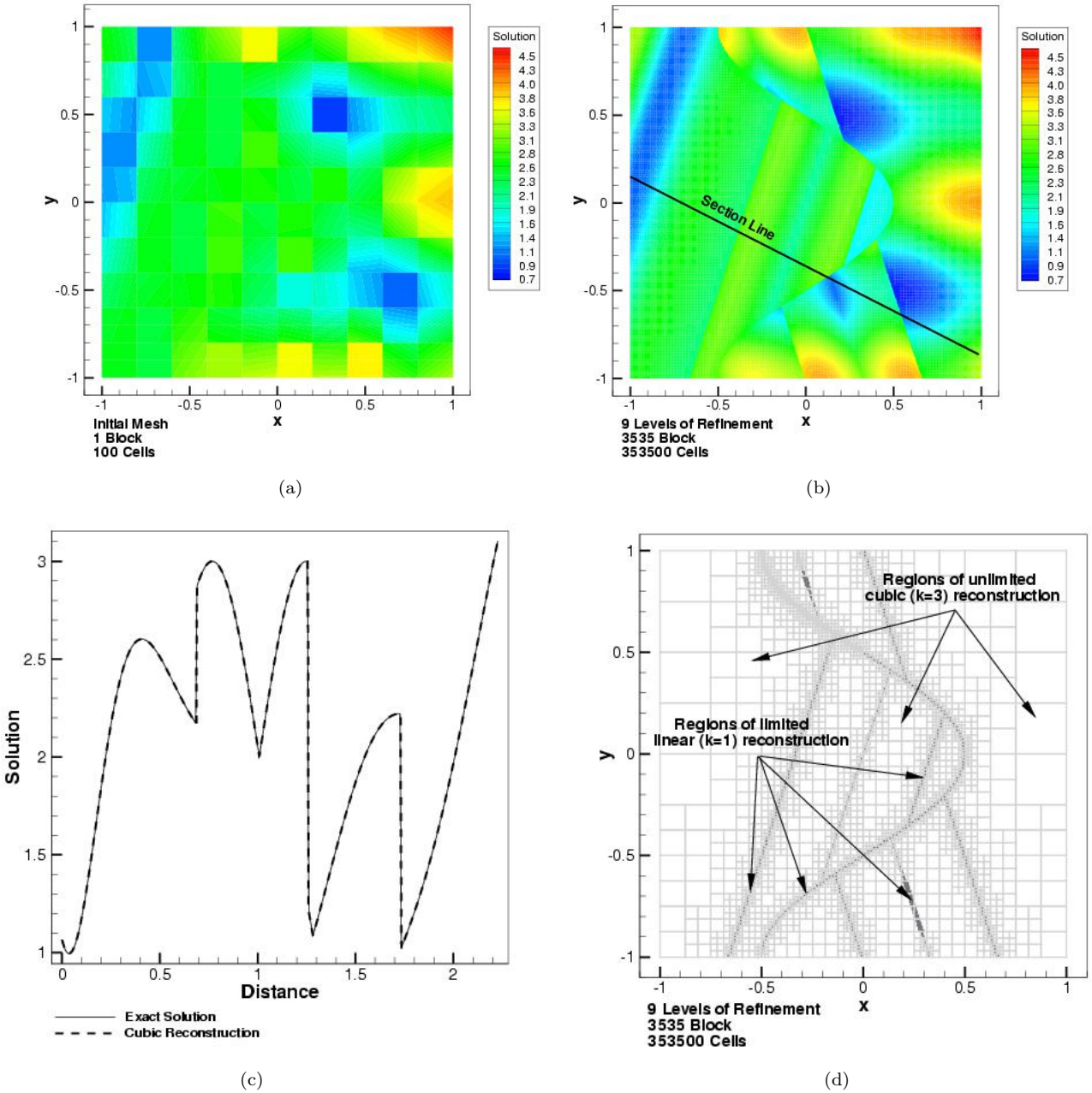

Figure 15. (a) Contour plot of a third-order ($k=3$) CENO reconstructed solution of the Abgrall's function on an initial uniform 10×10 Cartesian mesh consisting of 1 block and 100 computational cells; (b) the cubic reconstructed solution on the mesh obtained after eight mesh refinements which consists of 3,535 blocks and 353,500 cells; (c) Cross section of the cubic CENO reconstructed solution is compared against the exact solution of the Abgrall's function along the section line shown in (b); and (d) regions in which the CENO scheme uses unlimited cubic and limited linear reconstruction.

scheme in conjunction with the h-refinement criteria based on the smoothness indicator of the hybrid CENO reconstruction technique is capable of refining both under-resolved (in-accurate) and non-smooth regions of the solution and will not unnecessarily refine resolved solution content. The bow shock and shocks arising at the base of the cylinder are well identified by the smoothness indicator and well resolved by the AMR procedure.

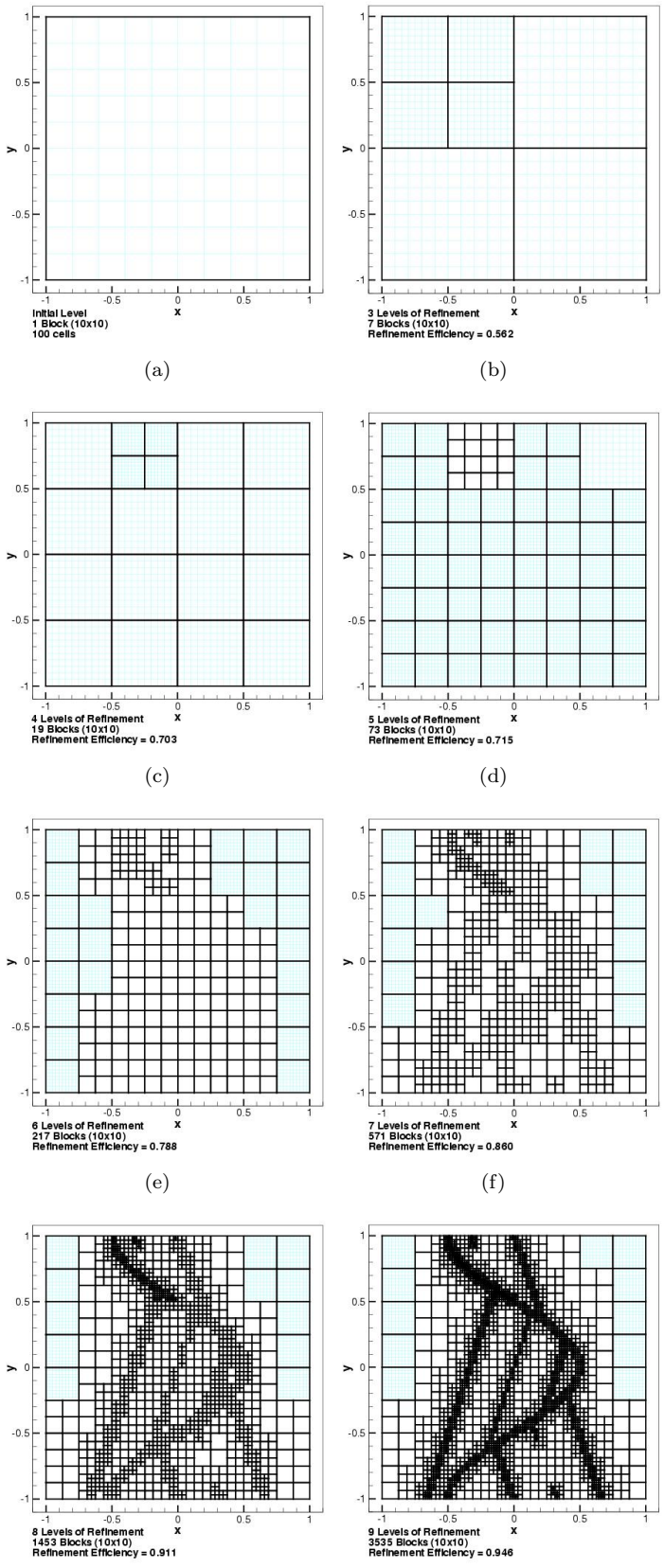

Figure 16. (a)-(h) Sequence of AMR meshes generated by the block-based refinement algorithm for the refinement of the Abgrall's function (refer to Fig. 15). The initial mesh (a) consisted of 1 block and 100 computational cells. The final mesh (h) had 3,535 blocks 10×10 and 353,500 cells with a refinement efficiency of $\eta=0.946$.

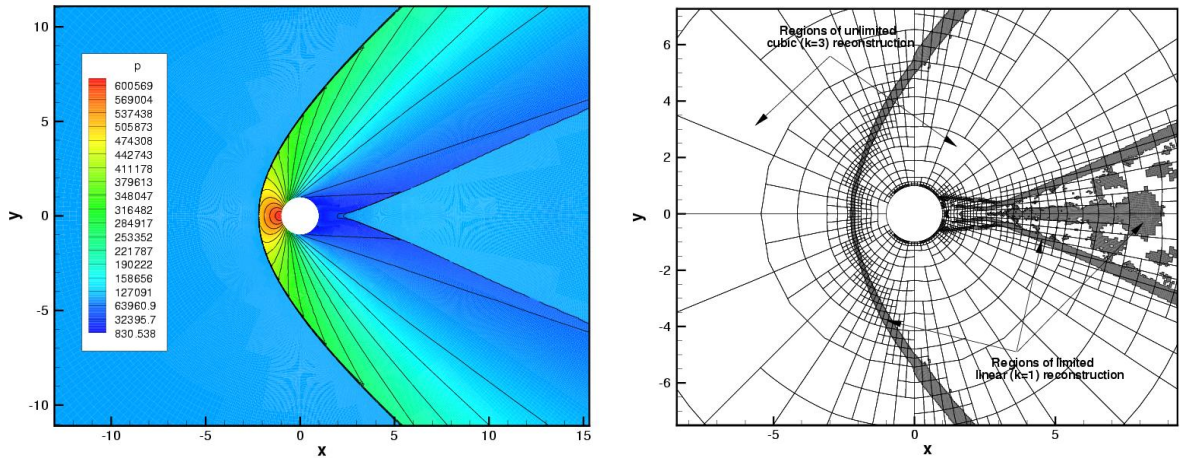

(a) (b)

Figure 17. (a) Predicted pressure distribution for $M = 2.1$ flow past a circular cylinder obtained using the 4th-order CENO scheme on the final refined AMR mesh; and (b) corresponding regions in which the CENO scheme uses unlimited cubic and limited linear reconstruction for $M = 2.1$ flow past a circular cylinder.

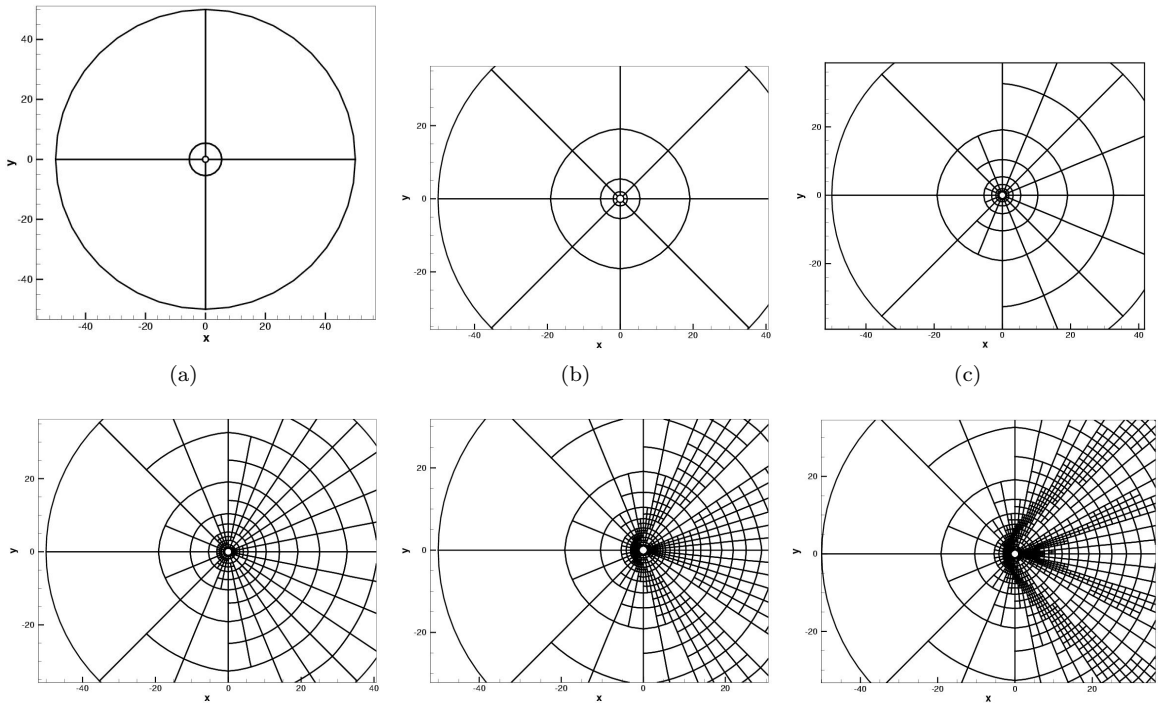

(a) (b) (c)

(d) (e) (f)

Figure 18. Sequence of adaptively refined AMR mesh for supersonic flow past a circular cylinder: (a) initial mesh with 8 10×10 blocks; (b) first refined mesh with 32 10×10 blocks; (c) second refined mesh with 110 10×10 blocks; (d) third refined mesh with 320 10×10 blocks; (e) fourth refined mesh with 908 10×10 blocks; (g) final refined mesh with 2150 10×10 blocks and refinement efficiency of $\eta = 0.737$.

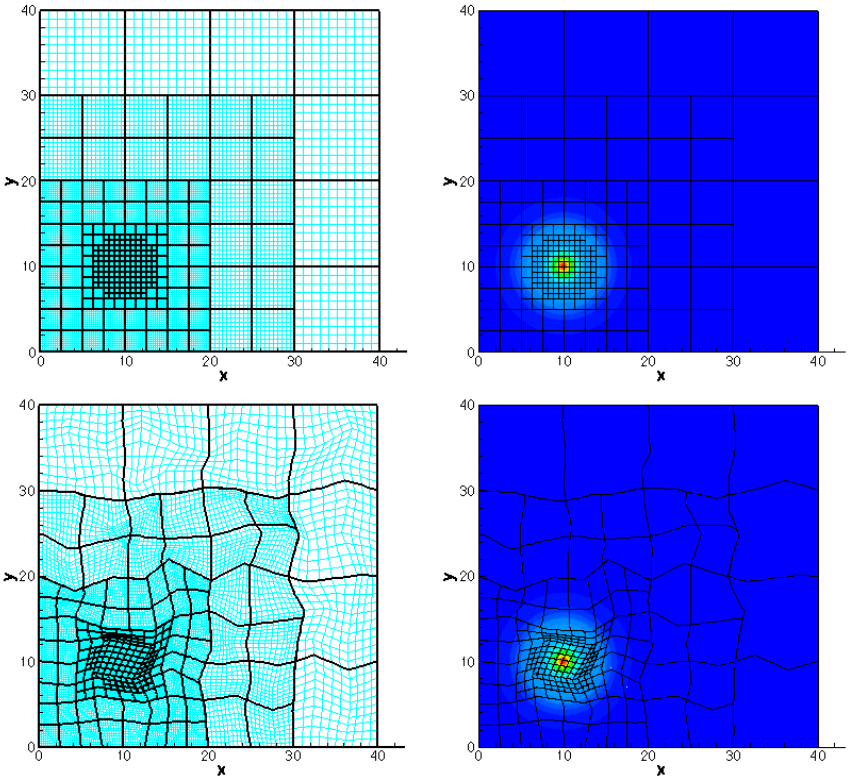

(a)

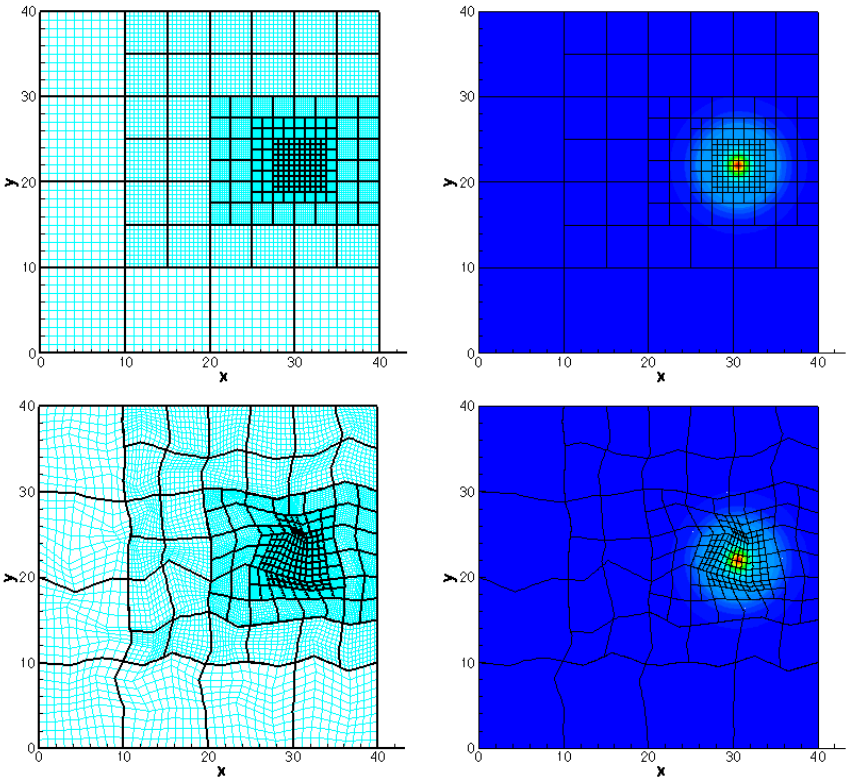

(b)

Figure 19. (a) Representation of initial density variation $\rho(\mathbf{x}) = 1 - \tanh^2(\mathbf{x} - \mathbf{x_o})$, $\mathbf{x_o}(10, 10)$, on the starting Cartesian and disturbed AMR meshes; (b) Final solution representation on both Cartesian and disturbed AMR meshes at the end of the advection.

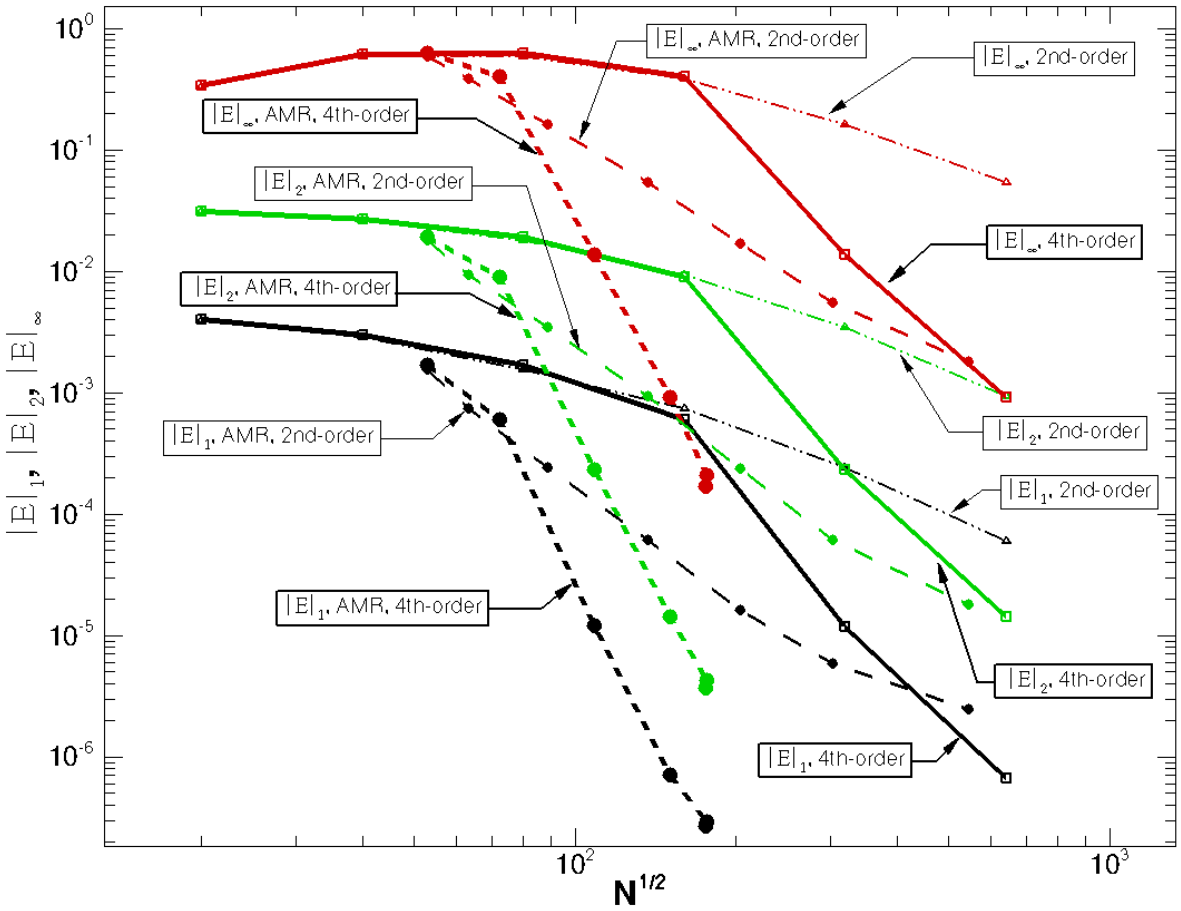

Figure 20. L_1, L_2 **and** L_∞ **norms of the error at the end of the advection (see Fig. 19b) as a function of mesh density obtained using a 2nd-order limited scheme and the 4th-order CENO method on both uniform and dynamically refined AMR Cartesian meshes.**

Finally, in order to estimate the accuracy of the CENO algorithm in conjunction with the AMR procedure, the linear advection of the density variation $\rho(\mathbf{x}) = 1 - \tanh^2(\mathbf{x} - \mathbf{x_o})$ from $\mathbf{x_o}(10, 10)$ along a 30° direction is considered in a rectangular box. The Mach number of the advecting flow is $M = 0.7$ and the final time of interest is $t = 100$ ms. The initial condition as well as the starting meshes are shown in Fig. 19a. In Fig. 19b it is shown the final solution and the meshes at the end of the advection. The error norms based on the error measurements at the end of the advection are shown in Fig. 20 for uniform and dynamically refined AMR Cartesian meshes. The plot of the error norms of this problem shows that for targeted solution accuracies less than 10^{-3}, the number of computational cells required by the 4th-order CENO scheme applied in conjunction with AMR is about 10 to 20 times smaller in each coordinate direction than what a limited 2nd-order scheme on uniform mesh would require. This would imply a reduction in mesh requirements by a factor of 100-400 for two-dimensional problems and by a factor of 1,000-8,000 in three dimensions, thus further demonstrating the great potential of the high-order AMR approach. The plot also reveals the fact that if low solution error is required, the high-order scheme on uniform mesh may require fewer computational cells than a 2nd-order method used in conjunction with AMR, which confirms Jameson's findings[2] mentioned earlier in the paper. Note that this comparison has not taken into account the computational costs of the AMR and high-order schemes as compared to their uniform mesh and low-order method counterparts. In particular, this was not attempted here due to inefficiencies in the time marching schemes which may lead to unfair comparisons.

VI. Discussion and Concluding Remarks

A new high-order CENO finite-volume scheme with AMR is proposed for solving hyperbolic systems of conservation laws on body-fitted multi-block mesh. The ability of the scheme to accurately represent solutions with smooth extrema and robustly handle under-resolved and/or non-smooth solution content (i.e., solutions with shocks and discontinuities) is demonstrated. The usefulness of an h-refinement criterion based on the smoothness indicator of the hybrid scheme has also been evaluated and shown to provide a robust and reliable mesh adaptation algorithm that is capable of refining both under-resolved (in-accurate) and non-smooth regions of the solution and will not unnecessarily refine resolved solution content. For large systems and multi-dimensional problems, the proposed CENO scheme would seem to provide high-order accuracy at a lower computational cost as compared to other similar approaches. Future work will include further investigation of the high-order CENO scheme, the efficient parallelization of the algorithm and extension to three-dimensional problems, and the application of the method to partial differential equations having elliptic behaviour.

Acknowledgements

This research was supported by a Premier's Research Excellence Award from the Ontario Ministry of Energy, Science, and Technology and by the Natural Sciences and Engineering Research Council of Canada (NSERC CRO Grant 260862-02). The first author would also like to thank the Government of Ontario for financial support received in the form of an Ontario Graduate Scholarship award. Funding for the parallel computing facility used to perform the computations described herein was obtained from the Canadian Foundation for Innovation and Ontario Innovation Trust (CFI Project No. 2169). The authors are very grateful to these funding agencies for their support.

References

[1]Moin, P. and Mahesh, K., "Direct numerical simulation: a tool in turbulence research," *Annu. Rev. Fluid Mech.*, Vol. 30, 1998, pp. 539–578.

[2]Jameson, L., "AMR vs. High Order Schemes," *Journal of Scientific Computing*, Vol. 18, 2003, pp. 1–24.

[3]Harten, A., Enquist, B., Osher, S., and Chakravarthy, S. R., "Uniformly High Order Accurate Essentially Non-Oscillatory Schemes, III," *Journal of Computational Physics*, Vol. 71, 1987, pp. 231–303.

[4]Abgrall, R., "On Essentially Non-Oscillatory Schemes on Unstructured Meshes: Analysis and Implementation," *Journal of Computational Physics*, Vol. 114, 1994, pp. 45–58.

[5]Sonar, T., "On the construction of essentially non-oscillatory finite volume approximations to hyperbolic conservation laws on general triangulations: polynomial recovery, accuracy and stencil selection," *Computer Methods in Applied Mechanics and Engineering*, 1997, pp. 140–157.

[6]Jiang, G.-S. and Shu, C.-W., "Efficient Implementation of Weighted ENO Schemes," *Journal of Computational Physics*, Vol. 126, 1996, pp. 202–228.

[7]Friedrich, O., "Weighted Essentially Non-Oscillatory Schemes for the Interpolation of Mean Values on Unstructured Grids," *Journal of Computational Physics*, Vol. 144, 1998, pp. 194–212.

[8]Hu, C. and Shu, C.-W., "Weighted Essentially Non-Oscillatory Schemes on Triangular Meshes," *Journal of Computational Physics*, Vol. 150, 1999, pp. 97–127.

[9]Stanescu, D. and Habashi, W., "Essentially Nonoscillatory Euler solutions on unstructured meshes using extrapolation," *AIAA Journal*, Vol. 36, 1998, pp. 1413–1416.

[10]Haselbacher, A., "A WENO Reconstruction Algorithm for Unstructed Grids Based on Explicit Stencil Construction," Paper 2005-0879, AIAA, January 2005.

[11]Wolf, W. R. and Azevedo, J., "High-Order Unstructured Essentially Nonoscillatory and Weighted Essentially Nonoscillatory Schemes for Aerodynamic Flows," *AIAAJ*, Vol. 44, No. 10, October 2006, pp. 2295–2310.

[12]Barth, T. J. and Fredrickson, P. O., "Higher Order Solution of the Euler Equations on Unstructured Grids Using Quadratic Reconstruction," Paper 90-0013, AIAA, January 1990.

[13]Barth, T. J., "Recent Developments in High Order K-Exact Reconstruction on Unstructured Meshes," Paper 93-0668, AIAA, January 1993.

[14]Cockburn, B. and Shu, C.-W., "TVB Runge-Kutta Local Projection Discontinous Galerkin Finite-Element Method for Conservation Laws II: General Framework," *Mathematics of Computation*, Vol. 52, 1989, pp. 411.

[15]Cockburn, B., Lin, S.-Y., and Shu, C.-W., "TVB Runge-Kutta Local Projection Discontinous Galerkin Finite-Element Method for Conservation Laws III: One-Dimensional Systems," *Journal of Computational Physics*, Vol. 84, 1989, pp. 90.

[16]Cockburn, B., Hou, S., and Shu, C.-W., "TVB Runge-Kutta Local Projection Discontinous Galerkin Finite-Element Method for Conservation Laws IV: The Multidimensional Case," *Journal of Computational Physics*, Vol. 54, 1990, pp. 545.

[17]Ollivier-Gooch, C. F., "High-Order ENO Schemes for Unstructured Meshes Based on Least-Squares Reconstruction," Paper 97-0540, AIAA, January 1997.

[18]Ollivier-Gooch, C. F., "Quasi-ENO Schemes for Unstructured Meshes Based on Unlimited Data-Dependent Least-Squares Reconstruction," *Journal of Computational Physics*, Vol. 133, 1997, pp. 6–17.

[19]Wang, Z. J., "Spectral (Finite) Volume Method for Conservation Laws on Unstructured Grids," *Journal of Computational Physics*, Vol. 178, 2002, pp. 210–251.

[20]Wang, Z. J., Zhang, L., and Liu, Y., "High-Order Spectral Volume Method for 2D Euler Equations," Paper 2003–3534, AIAA, June 2003.

[21]Liu, Y., Vinokur, M., and Wang, Z., "Discontinuous spectral difference method for conservation laws on unstructured grids," *Proceedings of the 3rd International Conference on Computational Fluid Dynamics, Toronto, Canada, July 12–16*, 2004.

[22]Sun, Y., Wang, Z. J., and Liu, Y., "Spectral (finite) volume method for conservation laws on unstructured grids VI: extension to viscous flow," *J. Comput. Phys.*, Vol. 215, No. 1, 2006, pp. 41–58.

[23]May, G. and Jameson, A., "High-Order Accurate Methods for High-Speed Flow," Paper 2005-5251, AIAA, 2005.

[24]May, G. and Jameson, A., "A Spectral Difference Method for the Euler and Navier-Stokes Equations on Unstructured Meshes," Paper 2006-304, AIAA, January 2006.

[25]Barad, M. and Colella, P., "A fourth-order accurate local refinement method for Poisson's equation," *Journal of Computational Physics*, Vol. 209, 2005, pp. 1–18.

[26]De Rango, S. and Zingg, D., "Higher-order spatial discretization for turbulent aerodynamic computations," *AIAAJ*, Vol. 39, 2001, pp. 1296–1304.

[27]Venkatakrishnan, V., Allmaras, S. R., Kamenetskii, D. S., and Johnson, F. T., "Higher Order Schems for the Compressible Navier-Stokes Equations," Paper 2003-3987, AIAA, June 2003.

[28]Sachdev, J. S., Groth, C. P. T., and Gottlieb, J. J., "A Parallel Solution-Adaptive Scheme for Predicting Multi-Phase Core Flows in Solid Propellant Rocket Motors," *International Journal of Computational Fluid Dynamics*, Vol. 19, No. 2, 2005.

[29]Harten, A. and Chakravarthy, S. R., "Multi-dimensional ENO schemes for general geometries," Report 91-76, ICASE, September 1991.

[30]Harten, A., "High Resolution Schemes for Hyperbolic Conservation Laws," *Journal of Computational Physics*, Vol. 49, 1983, pp. 357–393.

[31]Godunov, S. K., "Finite-Difference Method for Numerical Computations of Discontinuous Solutions of the Equations of Fluid Dynamics," *Matematicheskii Sbornik*, Vol. 47, 1959, pp. 271–306.

[32]Roe, P. L., "Approximate Riemann Solvers, Parameter Vectors, and Difference Schemes," *Journal of Computational Physics*, Vol. 43, 1981, pp. 357–372.

[33]Einfeldt, B., "On Godunov-Type Methods for Gas Dynamics," *SIAM Journal on Numerical Analysis*, Vol. 25, 1988, pp. 294–318.

[34]Linde, T. J., *A Three-Dimensional Adaptive Multifluid MHD Model of the Heliosphere*, Ph.D. thesis, University of Michigan, May 1998.

[35]Linde, T., "A practical, general-purpose, two-state HLL Riemann solver for hyperbolic conservation laws," *International Journal for Numerical Methods in Fluids*, Vol. 40, 2002, pp. 391–402.

[36]Gottlieb, J. J. and Groth, C. P. T., "Assessment of Riemann Solvers for Unsteady One-Dimensional Inviscid Flows of Perfect Gases," *Journal of Computational Physics*, Vol. 78, 1988, pp. 437–458.

[37]Lawson, C. and Hanson, R., *Solving least squares problems*, Prentice-Hall, INC, 1974.

[38]Venkatakrishnan, V., "On the Accuracy of Limiters and Convergence to Steady State Solutions," Paper 93-0880, AIAA, January 1993.

[39]Ollivier-Gooch, C. F. and Van Altena, M., "A High-order Accurate Unstructured Mesh Finite-Volume Scheme for the Advection-Diffusion Equation," *Journal of Computational Physics*, Vol. 181, No. 2, 2002, pp. 729–752.

[40]Northrup, S. A. and Groth, C. P. T., "Solution of Laminar Diffusion Flames Using a Parallel Adaptive Mesh Refinement Algorithm," Paper 2005-0547, AIAA, January 2005.

[41]Gao, X. and Groth, C. P. T., "A parallel adaptive mesh refinement algorithm for predicting turbulent non-premixed combusting flows," *International Journal of Computational Fluid Dynamics*, Vol. 20, No. 5, 2006, pp. 349–357.

[42]McDonald, J. and Groth, C. P. T., "Numerical Modeling of Micron-Scale Flows Using the Gaussian Moment Closure," Paper 2005-5035, AIAA, June 2005.

[43]Berger, M. J., "Adaptive Mesh Refinement for Hyperbolic Partial Differential Equations," *Journal of Computational Physics*, Vol. 53, 1984, pp. 484–512.

[44]Berger, M. J. and Colella, P., "Local Adaptive Mesh Refinement for Shock Hydrodynamics," *Journal of Computational Physics*, Vol. 82, 1989, pp. 67–84.

[45]Woodward, P. and Colella, P., "The Numerical Simulation of Two-Dimensional Fluid Flow with Strong Shocks," *Journal of Computational Physics*, Vol. 54, 1984, pp. 115–173.

[46]Coirier, W. J. and Powell, K. G., "An Accuracy Assessment of Cartesian-Mesh Approaches for the Euler Equations," *Journal of Computational Physics*, Vol. 117, 1995, pp. 121–131.